

The Effect of Powder Characteristics on Build Quality of High-Purity Tungsten Produced *via* Laser Powder Bed Fusion (LPBF)



A.C. FIELD, L.N. CARTER, N.J.E. ADKINS, M.M. ATTALLAH, M.J. GORLEY, and M. STRANGWOOD

Two high-purity tungsten powders, produced *via* different manufacturing techniques, were characterized to determine size distribution, morphology, thermal properties, and flow characteristics and, thus, the likely suitability for Laser Powder Bed Fusion (LPBF) production. Specimens from duplicate builds were produced with the two powders and characterized for density, defect mechanisms, and thermal penetration into the substrate plate to compare apparent power densities. The first powder was a chemically reduced powder with irregular morphology and the second, a plasma spheroidized powder with highly spherical morphology. The latter was found to have tighter morphological control and size distribution, having a third of particles at the modal particle size in comparison to a fifth of the chemically reduced powder. This led to better flow characteristics, and an increase of 1.5 g cm^{-3} (1500 kg m^{-3}) in the packing densities seen in the powder bed which corresponds to 57 pct theoretical density *vs* 50 pct theoretical density in the chemically reduced powder. As a result, the specimens produced from the plasma spheroidized powder had higher densities (97.3 *vs* 88.5 pct) and the dominant defect mechanism moved from lack of fusion dominated in the chemically reduced powder to cracking dominated in the plasma spheroidized. The plasma spheroidized powder also showed higher apparent power densities (effective absorptivities) as evidenced by an 80 pct deeper penetration of the laser into the substrate plate.

<https://doi.org/10.1007/s11661-019-05601-6>
© The Author(s) 2019

I. INTRODUCTION

TUNGSTEN is a candidate material for the plasma facing components (PFCs) within a nuclear fusion reactor as a result of its high melting point (3420 °C, 3695 K), high thermal conductivity ($164 \text{ W m}^{-1} \text{ K}^{-1}$), and high density (19250 kg m^{-3}).^[1] These allow the components to survive the operating temperatures as well as providing effective radiation shielding and conduction of heat through the components. The comparatively low activation of tungsten means that long-term waste storage does not need to be considered and recycling methods are possible after 75 years.^[2]

There are difficulties associated with the processing of tungsten however, as a result of its high melting point and intrinsic brittleness (Ductile–Brittle Transition Temperature (DBTT) $\sim 400 \text{ °C}$, 673 K).^[3] Conventionally, powder metallurgy methods including sintering have been used, but as final machining is challenging, the complexity of component geometries has been limited.^[4] The current divertor monoblock design can be seen in Figure 1; its simple shape is largely dictated by manufacturing issues.

Additive manufacturing techniques including Laser Powder Bed Fusion (LPBF) offer the potential to produce components with greater complexity, such as small internal cooling channels, and without the need for low melting point binders or sintering aids (*e.g.*, Cu, Ni).^[5] Early attempts at LPBF of tungsten-based materials investigated additions of these sintering aids which acted as a binder phase, lowering the melting point and increasing processability so that densities of around 80 pct with little cracking were achieved processing at 100 W.^[6,7] The high activation of Cu and Ni makes this strategy unsuitable for fusion applications. Attempts at processing both pure tungsten and molybdenum yielded low densities (< 85 pct) due to the low laser powers

A.C. FIELD is with the School of Metallurgy & Materials, University of Birmingham, Edgbaston, B15 2TT, UK and also with the UK Atomic Energy Authority, Culham Science Centre, Abingdon, Oxfordshire, OX14 3DB, UK. L.N. CARTER, N.J.E. ADKINS, M.M. ATTALLAH, and M. STRANGWOOD are with the School of Metallurgy & Materials, University of Birmingham. Contact e-mail: m.strangwood@bham.ac.uk M.J. GORLEY is with the UK Atomic Energy Authority, Culham Science Centre.

Manuscript submitted May 24, 2019.

Article published online January 1, 2020

(< 200 W) used [8,9] resulting in incomplete consolidation. More recent work, conducted with 300- to 500-W systems have shown improved results with densification up to 96 pct of theoretical density (TD), but suggested that cracking may be present.[10,11] Densities of 96 pct are significantly higher than previous attempts, but are still lower than those achievable in LPBF of conventional materials such as 316L where densities in excess of 99.5 pct are possible.[12]

Within radiation shielding applications, it is generally known that increasing the density of a material improves its shielding effect,[13] and as a result, improved densities are of importance to the successful implementation of LPBF technologies for the production of refractory metals. However, the presence of cracking as a result of fabrication would be detrimental in terms of stress concentrators and crack propagation and therefore an optimum may exist where a small amount of residual porosity exists.

Figure 2 summarizes the main input parameters affecting final build quality; these can be nominally divided into laser parameters, environment, and powder characteristics. Of interest in this study is the effect of powder characteristics on build quality particularly in regard to densification.

The characteristics of the powder play a significant role in the occurrence of defects within a part, and good flowability (free flowing coefficient, ff_c , > 10)[14] and high packing density (> 60 pct)[15] are noted to improve overall quality in terms of prevalence of lack of fusion defects. The packing density of powders is known to be affected by their morphology with spherical powders

having the highest packing density and irregularly shaped particles having a significantly lower one.[16] Lee and Zhang showed an increase in powder packing density increased the likelihood of a continuous melt track forming due to a more consistent powder layer preventing fluid instabilities and, thus, balling.[17] Spherical powder particles also exhibit better flowability, giving more uniform layer spreading during LPBF production.[18] Karapatis *et al.* found that typical packing densities within a powder bed vary between 40 and 60 pct dependent on powder morphology, with more spherical morphologies increasing packing density.[19] Packing densities on the lower end of the spectrum will lead to less uniform heat input, asymmetrical shrinkage, and greater irregularities in recoating powder in subsequent layers.[18]

Although the laser power can be controlled and measured by machine settings, the actual heat input to the build will vary with the absorptivity of the powder. The absorptivity of tungsten powders and solid tungsten plate has been assessed theoretically and experimentally. These are summarized in Table I, from which there is a lack of correlation and consistency in the values determined. As the heat input will affect melting, consolidation, and thermal profiles, a need exists to identify trends in this with powder and process characteristics that can be correlated with final build quality.

Large flat surfaces or facets in the polyhedral powder used in the study by Wang *et al.*[10] may more closely mimic a flat surface which Boley *et al.*[21] predicted would have an absorptivity of 0.4. Absorptivity was found experimentally to vary between 0.25 and 0.55 for 100 μm layers by Trapp *et al.*,[20] depending on laser power used and if the thresholds for melting or keyholing were achieved. Boley *et al.*[21] conducted absorptivity measurements on titanium powders from different vendors but found no significant difference in absorptivity. However, if both powders were produced using the same method, variations in morphology and absorptivity are likely to be small.[10,20,21] Boley *et al.* found that the absorptivity of a powder tends to increase with the square root of the absorptivity value for a flat surface of the fully dense material.

The thermal conductivity in powders is significantly lower than that of the bulk material due to the ineffective conduction through the gas voids between the particles. Increasing the packing density was found to increase the thermal conductivity as there are often a greater number of particles in contact per unit area for conduction and therefore a smaller proportion of interparticle area.[22]

As seen in Table I, thus far investigations into absorptivity have largely been limited to different packing distributions,[21] materials, and effect of LPBF process parameters on absorptivity.[20,21] While studies have investigated powder absorptivity of tungsten, the experimental limitations including the partial sintering of powder, larger layer thicknesses than typical LPBF systems may diminish its applicability to LPBF fabrication.[10] Additionally, much of the energy absorbed will heat the powder to below the melting point of the material, which is ineffective to the LPBF process.

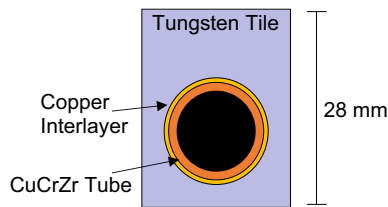


Fig. 1—Schematic representation of a divertor monoblock.

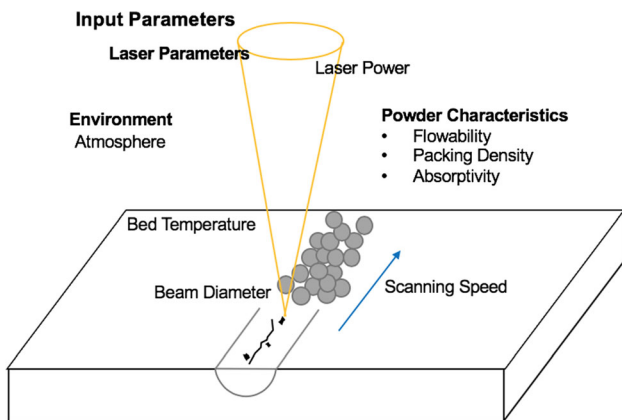


Fig. 2—Schematic diagram showing input parameters that will affect build quality.

Table I. Summary of Reported Laser Absorptivity Values

Study	Powder Morphology/Preparation Method	Experimental Method	Absorptivity	Comments
Wang <i>et al.</i> ^[10]	plasma spheroidized polyhedral	temperature increase measured from insulated base plate with pre-deposited powder during laser irradiation	0.68 0.5	powder pre-deposited on plate not representative of LPBF temperature increases of < 1000 K, well below melting point of tungsten laser wavelength of 1 μm
Boley <i>et al.</i> ^[21]	spherical (Gaussian distribution) flat plate irregular	modeled-ray trace calculations of the laser through Fresnel reflections until power reaches 0.01 pet incident power a thin layer of powder in a refractory metal disk ($\varnothing \sim 1 \text{ cm}$) with thermal insulation and thermocouples beneath the disk to measure temperature increase during laser irradiation	0.63 0.4 0.81	laser wavelength 970 nm layer thickness of 100 μm Trapp <i>et al.</i> found increased powder thickness increase number of reflections and increase absorptivity
Trapp <i>et al.</i> ^[20]	flat plate	temperature increase during laser irradiation measured on 0.5-mm-thick disk of tungsten ($\varnothing 10 \text{ mm}$) within a porous alumina holder for thermal isolation with thermocouples attached to disk base	0.25–0.55	laser scanning speed 1500 mm/s power variation 50–500 W Yb-fiber laser 65 μm absorptivity varied dependent on conduction or keyholing mode

This study will therefore aim to provide a method to analyze the minimum effective energy absorbed from the two powders by analyzing build plate penetration. This negates the issue of non-representative powder packing and due to the comparative nature of the study, the effects of heat losses to the system are limited as the gas flow, plate thickness, and resulting conductive and convective losses will be comparable with both powder builds.

II. EXPERIMENTAL METHOD

A. Sample Production

Two different, high-purity (< 99.88 wt pct) tungsten powders were used in this study, which were a chemically reduced (CR) powder supplied by H.C. Starck GmbH and a plasma spheroidized (PS) powder from LPW Technology Ltd., with nominal size distributions of < 105 μm and 30 to 60 μm , respectively. From manufacturer's specifications, the levels of expected impurities in the powders are summarized in Table II and of these impurities, it is oxygen that is likely to have the most significant effect.

Each powder was used to produce fourteen $10 \times 10 \times 10 \text{ mm}^3$ cubes using a narrow range of build parameters (duplicate builds of seven sets of parameters, Table III (with sample codes) laser power: 275 to 400 W; scan speed: 700 to 1250 mm s^{-1} ; and scan spacing: 0.06 to 0.075 mm, which allowed location-specific variations to be assessed). These were produced on a Concept M2 Laser Cusing machine fitted with a 400-W laser under an argon atmosphere containing approximately 200 ppm of oxygen.

A 2-mm-thick tungsten sheet (99.97 pct) supplied by Plansee was cut to size and attached to a $90 \times 90 \text{ mm}$ titanium substrate plate using a high-temperature metal adhesive to act as the build substrates for these cubes. The range of parameters used was selected to provide a range of heat inputs to the powders and have been quantified initially using the area energy density (AED).

AED is based on the laser power and the time needed to scan the entire area of the build plane, taking into account the overlap between scan tracks. In time δt , the laser would input an energy of $P \delta t$, and traverse a distance of $v \delta t$, see Figure 3.

So, in time δt , the area scanned by the laser corresponds to Eq. [1]:

$$\text{Scan area} = 2r \cdot v\delta t + r^2. \quad [1]$$

As δt increases, the approximation in Eq. [2] holds.

$$2r \cdot v\delta t + r^2 \rightarrow 2r \cdot v\delta t. \quad [2]$$

Therefore, the area energy density (AED; J mm^{-2}) was calculated using Eq. [3].

$$\text{AED} = \frac{P}{2r \cdot v}, \quad [3]$$

where P is laser power (W), v is laser scanning speed (mm s^{-1}), and r is laser spot radius (mm).

B. Powder Characterization

The oxygen contents in the two powders were determined *via* inert gas fusion using a LECO ONH836 machine, conducted by AMG Superalloys. A sample of material (0.1 to 0.1 g) was placed inside a graphite crucible with nickel flux. The sample was then fused releasing oxygen species which react with the carbon in the crucible to form carbon monoxide and carbon dioxide which was then detected and quantified using an NDIR (non-dispersive infrared) sensor.^[23]

The sizes of the particles were determined by Laser Particle Size Distribution (LPSD), conducted on a Sympatec GmbH HELOS system fitted with a SUCCELL wet dispersing system in accordance with ASTM D4464.^[24] Given the expected size distribution of the powder, an R2 lens with a detection range of 0.1 to 87.5 μm was used. $\text{Na}_4\text{P}_2\text{O}_7$ was added to the suspension of powder in distilled water to prevent agglomeration. The particle size distributions were confirmed *via* image analysis of backscattered electron (BSE) images obtained from a Hitachi TM3030 scanning electron microscope (SEM) operating at 15 kV. A visual investigation of the powder was also conducted to compare the morphology of the two powders; several images were taken at low magnification to allow several hundred particles to be analyzed. Higher magnification images were taken to provide greater detail.

Shear ring testing was conducted on a Schulze Shear Ring Tester RST-01 fitted with a small cell (Type S). Instantaneous tests were performed in accordance with ASTM D6773.^[25] This test was used to determine free flowing coefficient (ff_c) which is the ratio of consolidation stress to unconfined yield stress. A value greater than 10 for ff_c is considered to be free flowing and this is therefore the desired threshold for good powder flowability in LPBF.^[14]

The apparent density (ρ_A) of the powders was also determined in accordance with ASTM B212.^[26,27] The pack density term in LPBF is equivalent to the bulk or apparent densities of the powders. The value can also be as a percentage of the density of solid material (19,300 kg m^{-3} for tungsten) for easier comparison especially between material systems.

C. Sample Characterization

Following production, most samples were removed from the tungsten substrate plate using a wire EDM and subjected to Archimedes' density testing (ASTM B962).^[28]

The build orientations with respect to the substrate and deposit can be seen in Figure 4. Samples were then sectioned in the mid-plane, parallel to the substrate plate and polished to a 0.03- μm finish with colloidal silica (XY section). Defect quantification of the polished surfaces, as observed using an optical microscope (Zeiss Axioscop-2 equipped with Axiovision 4.6.3 image capture and analysis software), was conducted using Fiji

Table II. Maximum Expected Impurity Levels (ppm)

	W	Al	Ca	Cr	Cu	Fe	Mo	Ni	Si	Ta	O
Chemically Reduced	bal.	30	20	100	10	200	100	150	50	—	170*
Plasma Spheroidized	bal.	—	—	10	—	10	30	10	—	30	370*

*Determined *via* inert gas fusion.

Table III. Sample List and Build Parameters Used

Sample Code	Powder	Power (W)	Laser Beam Radius (μm)	Scan Speed (mm s^{-1})	Scan Spacing (mm)	AED (J mm^{-2})
PS-A	PS*	300	42	950	0.06	3.76×10^{-3}
PS-B	PS	300	42	750	0.06	4.76×10^{-3}
PS-C	PS	400	44.5	1250	0.06	3.60×10^{-3}
PS-D	PS	300	42	750	0.075	4.76×10^{-3}
PS-E	PS	300	42	850	0.06	4.20×10^{-3}
PS-F	PS	300	42	850	0.075	4.20×10^{-3}
PS-G	PS	275	40	700	0.06	4.91×10^{-3}
CR-A	CR*	300	42	950	0.06	3.76×10^{-3}
CR-B	CR	300	42	750	0.06	4.76×10^{-3}
CR-C	CR	400	44.5	1250	0.06	3.60×10^{-3}
CR-D	CR	300	42	750	0.075	4.76×10^{-3}
CR-E	CR	300	42	850	0.06	4.20×10^{-3}
CR-F	CR	300	42	850	0.075	4.20×10^{-3}
CR-G	CR	275	40	700	0.06	4.91×10^{-3}

*PS and CR represent the Plasma Spheroidized and Chemically Reduced powders, respectively.

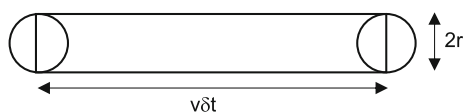


Fig. 3—Schematic representation of the laser scan parameters related to AED.

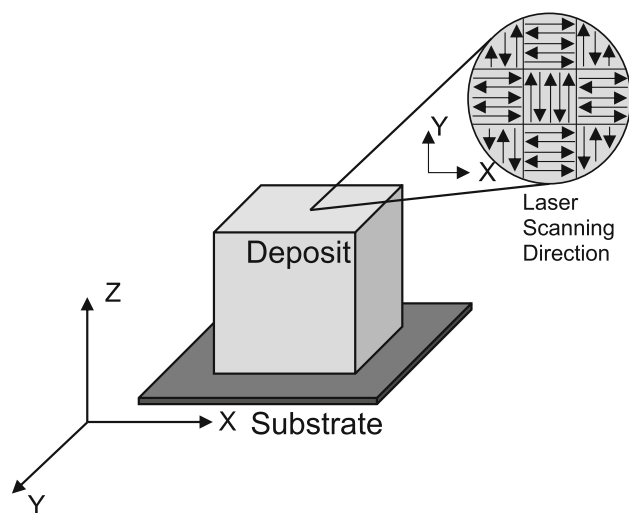


Fig. 4—Schematic showing the deposit and substrate, laser scanning directions, and build orientations.

software to determine the area fraction of defects on a binary image. Based on manual measurements of small lack of fusion defects, a threshold size of $1800 \mu\text{m}^2$ was used, with defects larger than this determined to be lack

of fusion defects, and those smaller determined to be cracks(see Figure 5).^[29]

A section was also taken perpendicularly through both substrate plate and deposit for samples CR-B and PS-B to determine the penetration depth of the fusion zones into the build plate for the two powder types (XZ section). These were taken from the same place in the build plate and were prepared in the same way for optical microscopy and image analysis. Measurements were taken manually using the lowest visible boundary between the parent material and the fusion zone from a datum of the substrate plate level away from the deposit at least every 0.5 mm using Fiji software across the width of the deposit,^[29] see Figure 6.

III. RESULTS AND DISCUSSION

Archimedes' density testing was conducted on the samples produced *via* LPBF; Figure 7 shows the variation of sample density as a function of AED.

As a narrow range of build parameters close to the optimum was used for the builds, there are only slight variations in sample density indicated in Figure 7. Indeed, the range from highest to lowest values for density was around 5 pct for the chemically reduced powder and less than 2 pct for the plasma spheroidized powder. Hence, no strong trends can be seen in terms of the effect of process parameters on sample density. There appears to be a large decrease in the density for samples prepared from chemically reduced powder from AED values of 3.6×10^{-3} to $3.76 \times 10^{-3} \text{ J mm}^{-2}$, but that appears to be a secondary effect compared with the differences in density between the two powder types.

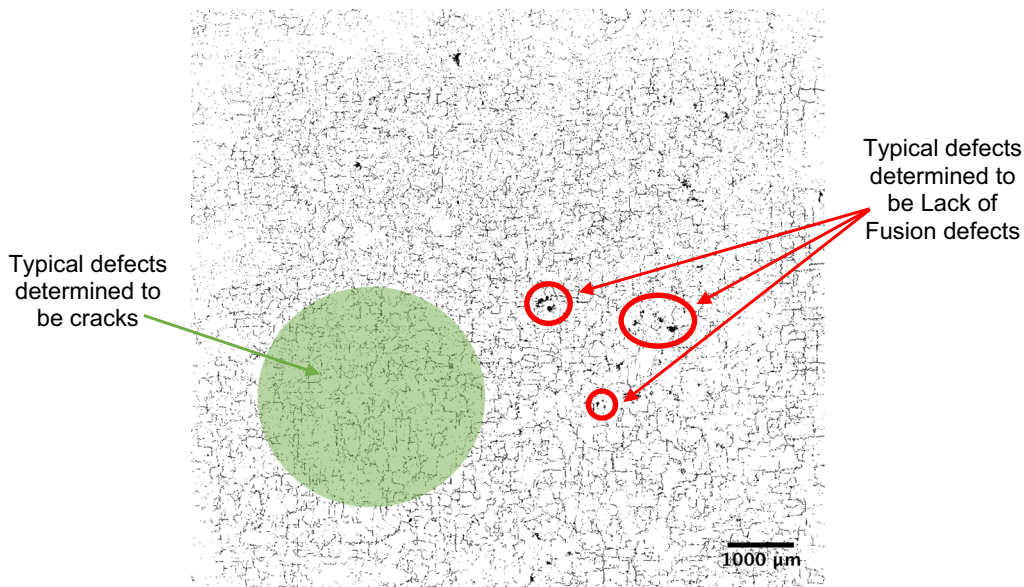


Fig. 5—Binary optical image of sample CR-C showing defects; those larger than $1800 \mu\text{m}^2$ determined to be lack of fusion defects, and those smaller determined to be cracks.

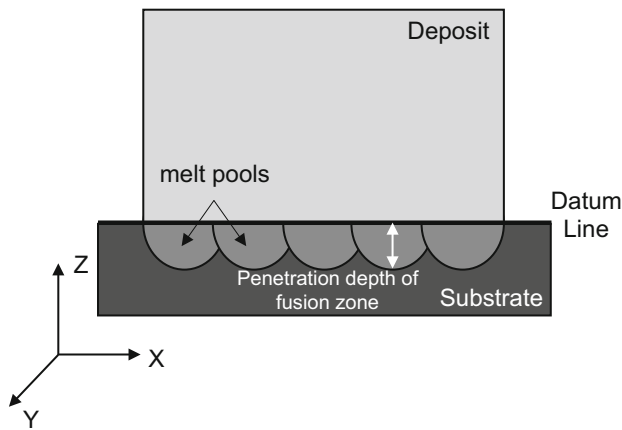


Fig. 6—Schematic of the build plate section showing penetration depth measurements taken.

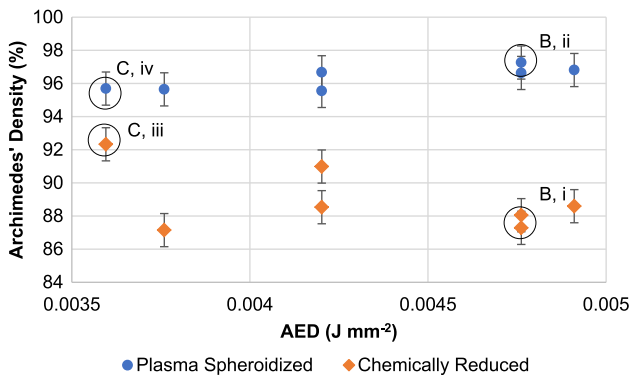


Fig. 7—Variation of sample density as a function of AED with points for the B and C samples of chemically reduced and plasma spheroidized powders circled.

However, while the density of the plasma spheroidized samples show a weak increase with increasing AED, that for the compacts made from the chemically reduced powder decreases. This results in the difference in density between compacts increasing from 4 to 10 pct (those produced from the plasma spheroidized powder having the greater density).

From the measured densities, two conditions for each powder were identified for further study. These can be seen circled and labeled (i) to (iv) (CR-B, PS-B, CR-C, and PS-C) in Figure 7. The conditions of interest were those which yielded the highest densities for compacts from the plasma spheroidized and chemically reduced powders and the same parameters applied to the other powder type, *i.e.*, samples CR-B, PS-B, CR-C, and PS-C. Of note, the optimum AED value for the compacts made from the plasma spheroidized powder corresponded to a power input of 300 W in comparison to the machine capability limit of 400 W required for compacts from the chemically reduced powder. The data in Figure 7 include samples deposited with the same AED value (Eq. [3]), but which have different Archimedes density values. These samples differ in their scan spacing—the lateral separation of one laser track from the next—and so would change the heat flow and temperature profiles in the build. This aspect has not been investigated systematically here, but its impact on build quality does need to be addressed, so that a more discriminating parameter than AED (Eq. [3]) can be determined.

Archimedes' density testing does not identify the types of defect present, it merely gives an indication of overall build quality. To better understand the defect distributions in the compacts, mounted sections were imaged. Figure 8 shows micrographs typical for each of the

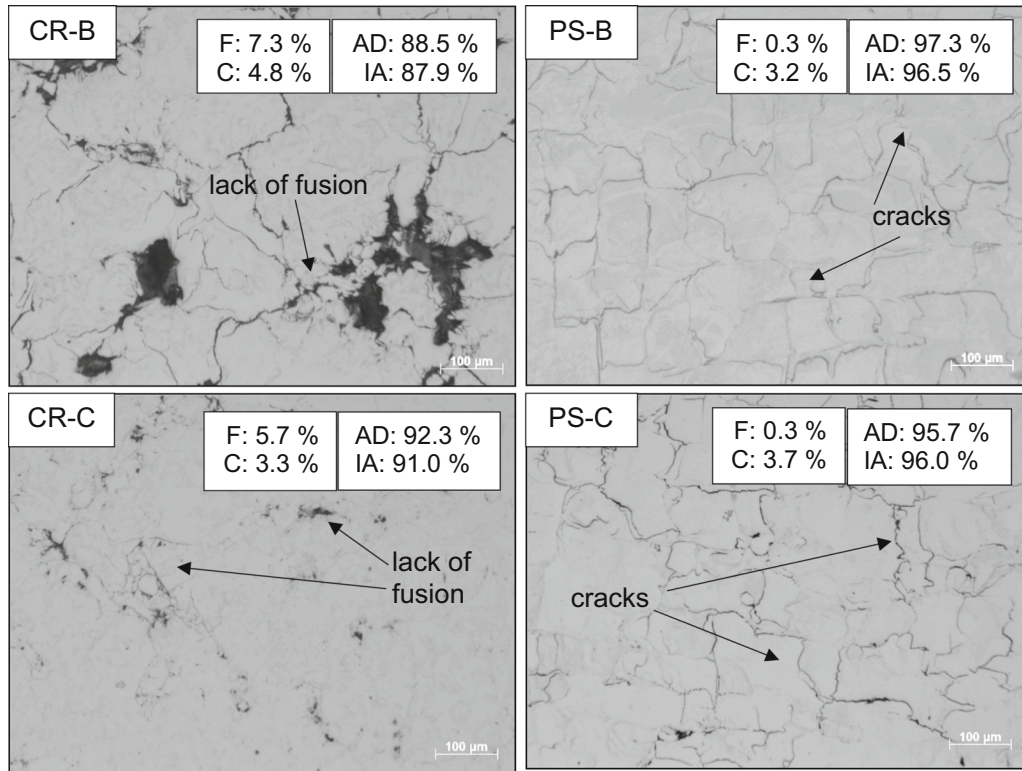


Fig. 8—Micrographs of (a) the plasma spheroidized powder from LPW Technology and (b) the chemically reduced powder from H.C. Starck.

Table IV. Comparison of Tungsten Powders Following Characterization

Powder	Apparent Density (g cm^{-3})	Percentage Density (Pct)	ff_c
Plasma Spheroidized	11.06	57.0	11.04
Chemically Reduced	8.64	44.5	9.59

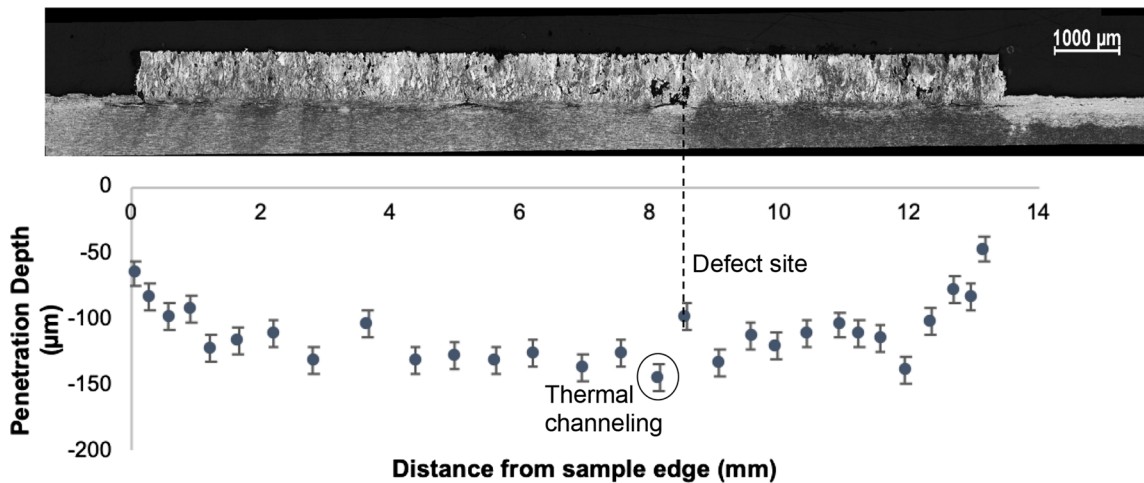


Fig. 9—Graph to show the size distribution of the plasma spheroidized and chemically reduced powders as determined by LPSD.

samples of interest sectioned parallel to the build plate along with the densities determined by Archimedes' (AD) and Image Analysis (IA) methods. An indication

of the proportion of lack of fusion (F) and cracks (C) was also determined through image analysis. Each pixel corresponds to $3 \mu\text{m}$ in the micrograph; each manual

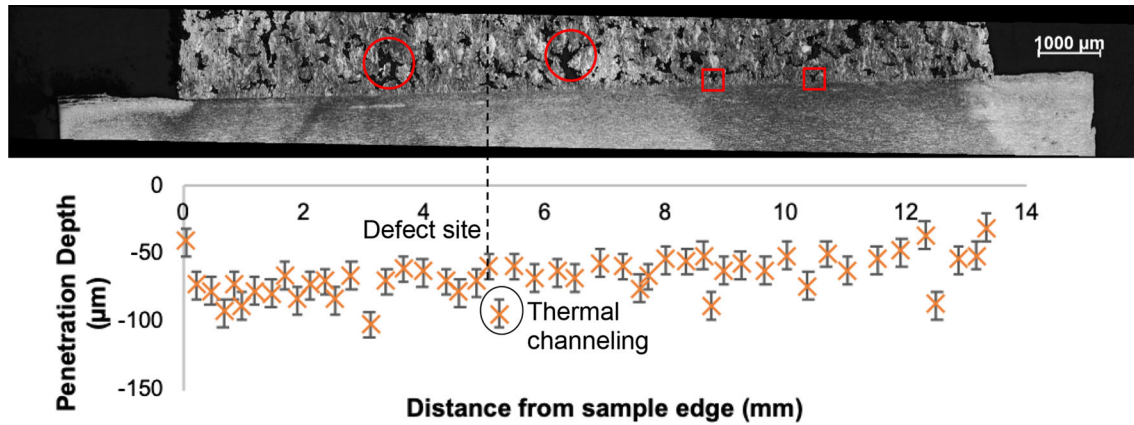


Fig. 10—Micrograph of section through the substrate plate and deposit produced using chemically reduced powder (CR-B) and the measured depth of the fusion zone at the corresponding position on the sample.

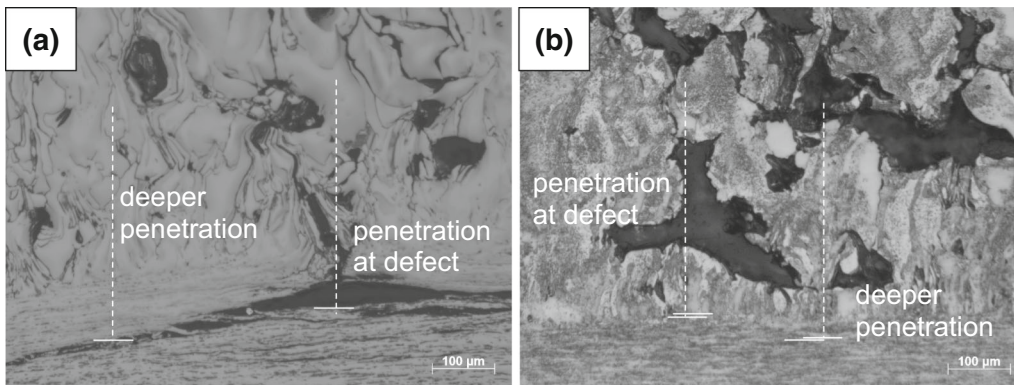


Fig. 11—Optical micrographs showing variation in penetration depth around areas of defects in build from (a) plasma spheroidized powder (PS-B) and (b) chemically reduced powder (CR-B).

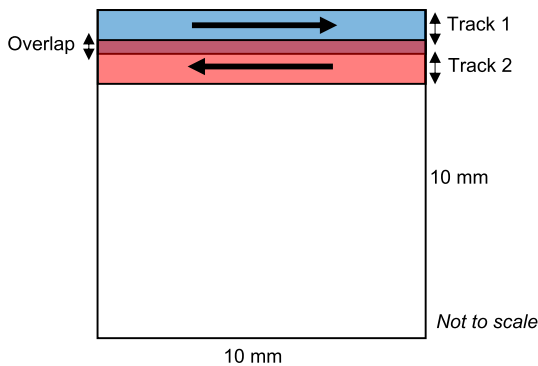


Fig. 12—Schematic diagram of scanning strategy and overlap.

measurement is accurate to the nearest 2 pixels, and the manual measurements had a minimum size of $1800 \mu\text{m}^2$, which corresponds to an error of approximately 0.5 pct. The void type defects were determined to be lack of fusion rather than porosity due to their irregular shape and large size. Gas or keyhole pores are typically spherical in shape. The high prevalence of large lack of fusion defects in CR-B may also lead to an increase in cracking as the defects may encourage crack initiation as their irregular shape could act as a stress concentrator.

Both from the micrographs themselves and the values indicated from image analysis, it can be seen that the samples produced from the chemically reduced powder in Figure 8 CR-B and CR-C have higher levels of lack of fusion, whereas the plasma spheroidized samples PS-B and PS-C are dominated by cracking, but the absolute amount of cracking, likely occurring on cooling, is consistent between 3 to 5 pct throughout the samples. Under optimal conditions for this powder, the compacts produced from the plasma spheroidized powder can be considered to be nominally dense with only 0.3 pct lack of fusion voids. The quantity of cracking observed in the mid-build XY plane section results in only ~ 97 pct theoretical density being achieved and likely occurs during the rapid cooling to which all samples were subjected rather than a parameter-specific variation. The effects of these different defect types on mechanical properties need to be determined; this study is concentrating on how their proportions change with powder type and processing conditions (albeit in a small window).

Variation in packing density is likely to affect the thermal diffusivity and possibly the laser absorptivity as discussed in the introduction, with the experimental set-up and powder layer thickness having an effect on

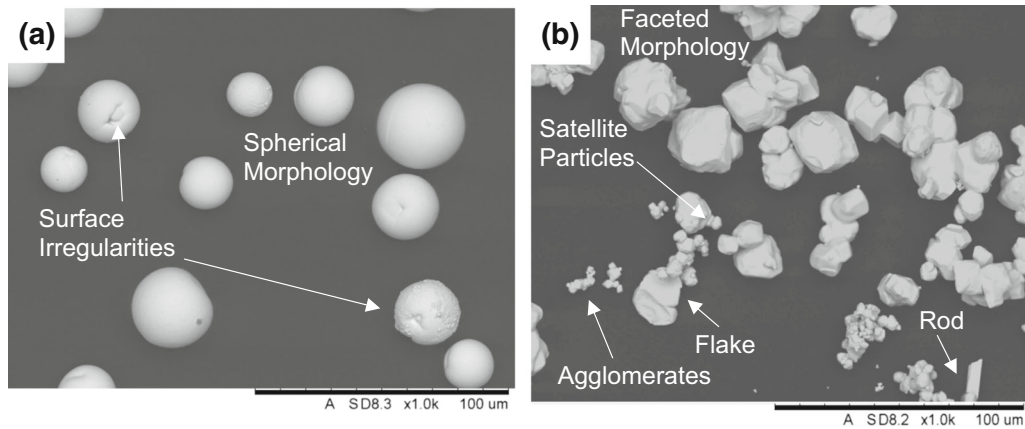


Fig. 13—Micrographs of (a) the plasma spheroidized powder from LPW Technology and (b) the chemically reduced powder from H.C. Starck.

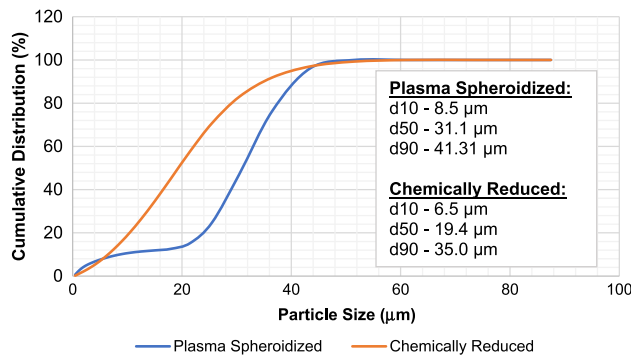


Fig. 14—Graph to show the size distribution of the plasma spheroidized and chemically reduced powders as determined by LPSD.

the packing density seen. In this study, the two powders were found to have noticeably different characteristics in terms of packing and flowability (see Table IV). The improved flowability and higher packing of the spherical powder would be expected to result in improved build quality with higher density. From Figure 7, this can be confirmed, with the plasma spheroidized powder producing samples with consistently higher density. This is possibly due to the higher packing density resulting in greater contact between the particles allowing for more heat flow through the powder.^[16,22]

To confirm this, the penetration depths of the fusion zone into the substrate material were measured (see Figures 9 and 10). The samples used for this were PS-B and CR-B, respectively, and therefore the build parameters were 300 W power, 750 mm s^{-1} scanning speed, and a scan spacing of 60 μm . The average penetration depth, excluding the edge 2 mm, of the sample for the plasma spheroidized powder is $122 \pm 10 \mu\text{m}$ compared with $67 \pm 10 \mu\text{m}$ for the deposit produced from the chemically reduced powder, corresponding to a 1.8 times greater penetration for the plasma spheroidized deposit. Both samples show some large defects, although, in line with the Archimedes density values and the mid-build XY sections, these were much larger

and numerous for CR-B compared with PS-B. Direct correlation of different 2D sections with each other and with a 3D measure will not be exact, but the trends shown are consistent. As penetration depth is being considered here, then those defects close have been studied in more detail.

Underneath the sites of defects close to the base plate, the penetration depth is smaller due to reduced thermal conduction through the void (see dashed line). There is also some evidence of deeper penetration before and after the defect (see circled points in Figures 9 and 10) consistent with channeling of the heat through the solid material around the void, deepening the fusion zone. In Figure 11, this can be seen more clearly with penetration deepening on increasing distance from defect sites. In order to see this effect, the defect had to form very close to the substrate plate. In the deposit produced from the chemically reduced powder (Figure 10), two large lack of fusion defects can be seen (circled) but were too far away from the base plate to see the effect of channeling, whereas the much smaller lack of fusion defects (indicated by a square) showed some channeling.

IV. DISCUSSION

The penetration depths are a measure of the fusion boundary for laser scanning of the first powder layer and, as such, is a measure of the heat absorbed by the powder from that layer.

Assuming that the region of average penetration is subject to one-dimensional heat flow (vertically downward in Figures 9 and 10) then the penetration depth can be used as an estimate of the minimum heat input into the powder. This will be an under-estimate of the total heat input, but as the scan rates and overlaps are the same, the amount of heat required to raise the substrate temperature for $T < T_m$ will be the same for both powder types. The minimum heat absorption can be determined as a function of the total energy input by the laser.

From Figure 12,

$$\begin{aligned}
\text{Area scanned} &= \text{length of track} \times \text{number of tracks} \\
&\times 2r \text{Number of tracks} = \text{sample width}/ \\
&\text{scan spacing} \text{Area scanned, } A = 10 \\
&\times (100/0.06) \times 0.084 = 140 \text{ mm}^2 \\
&= 1.4 \times 10^{-4} \text{ m}^{-2}
\end{aligned}
\tag{4}$$

The energy input over one layer will be the product of the area energy density (J m^{-2}) and the area (m^2) given by Eqs. [5] and [6].

$$E = \frac{P}{2r \cdot v} \times A \tag{5}$$

$$E = \frac{300}{2 \times (4.2 \times 10^{-5}) \times 0.06} \times \approx 666 \text{ J (3s.f.)} \tag{6}$$

Thus, the incident energy of the laser approximates to 666 J [to 3 significant figures (s.f.)].

The average penetration depths, d , from the two powders, are then used along with the layer thickness, h , of the powder, the apparent, ρ_A , and theoretical densities, ρ_T , of the powders and the layer area, A_{layer} , to determine the volume of the material where the maximum temperature was greater than or equal to its melting point, Eq. [7].

$$V = A_{\text{layer}} \cdot (d + h\rho_A/\rho_T) \tag{7}$$

For the plasma spheroidized powder, the volume was determined by Eq. [8].

$$\begin{aligned}
V &= 1 \times 10^{-4} \\
&\times \left(1.22 \times 10^{-4} + \left(3 \times 10^{-5} \times \frac{11.06}{19.3} \right) \right) \\
&\approx 1.39 \times 10^{-8} \text{ m}^3 \text{ (3 s.f.)}
\end{aligned}
\tag{8}$$

For the chemically reduced powder, the volume was determined by Eq. [9].

$$\begin{aligned}
V &= 1 \times 10^{-4} \times \left(6.7 \times 10^{-5} + \left(3 \times 10^{-5} \times \frac{8.64}{19.3} \right) \right) \\
&\approx 8.04 \times 10^{-9} \text{ m}^3 \text{ (3 s.f.)}
\end{aligned}
\tag{9}$$

Using the molar volume of tungsten, taken to be $9.55 \times 10^{-6} \text{ m}^3 \text{ mol}^{-1}$,^[30] the numbers of moles, n , for the two powders were determined using Eqs. [10] and [11].

$$n_{\text{PS}} = \frac{V}{V_m} = \frac{1.39 \times 10^{-8}}{9.55 \times 10^{-6}} \approx 1.46 \times 10^{-3} \text{ mol} \tag{10}$$

$$n_{\text{CR}} = \frac{V}{V_m} = \frac{8.04 \times 10^{-9}}{9.55 \times 10^{-6}} \approx 8.42 \times 10^{-4} \text{ mol} \tag{11}$$

The change in enthalpy, H , can be determined through the integration of the specific heat capacity, C_p , between the limits, T_m and T_0 , and the latent heat of fusion, L_f , Eq. [12].

$$H = \int_{T_0}^{T_M} C_p T + L_f \tag{12}$$

The specific heat capacity as a function of temperature was calculated using Eq. [13] with data from Reference 31.

$$\begin{aligned}
C_p &= 0.0032426 \left(1 - \frac{4805}{T^2} \right) + (2.1773 \times 10^{-6}) T \\
&+ (5.52461 \times 10^{-13}) T^3 \text{ cal g}^{-1} \text{ K}^{-1}
\end{aligned}
\tag{13}$$

The latent heat of fusion (L_f) was taken to be 46,000 J mol^{-1} ,^[30] which gives Eq. [14].

$$\begin{aligned}
\int_{293}^{3695} C_p T &\approx 150.3 \text{ cal g}^{-1} \equiv 629.0 \text{ J g}^{-1} \\
&\equiv 115637.9 \text{ J mol}^{-1}
\end{aligned}
\tag{14}$$

Assuming conversion factors of 1 cal. $\equiv 4.184 \text{ J}$ ^[32] and the atomic mass of tungsten of 183.84 J mol^{-1} ,^[30]

The enthalpy increases for the volumes of the two powders were found to be 236 and 136 J (3 s.f.) for the plasma spheroidized and chemically reduced powders, respectively. The relative minimum absorbed energies can then be compared to the incident energy of the laser in the two cases, 666 J. This results in a minimum absorption efficiency of 0.35 and 0.20 (2 s.f.), respectively.

The value of laser absorptivity will depend on material, powder characteristics (packing density and morphology), and processing environment.^[33] The samples studied in this work were processed under nominally identical conditions so that differences in effective laser absorptivity can be assumed to be due to powder composition, morphology, and packing density. From Table II, the different powder compositions differ only in their impurity levels, so that, unless vaporization losses cause the local environment to vary and modify its interaction with the laser beam then it is the powder geometry that is responsible for this difference. Although easily vaporized metallic elements such as Al, Cu, and Mo are present and differ between the powders, their low levels justify this assumption that powder composition variations are not significant.

Morphology and packing of particles can alter the contact area between adjacent particles and hence the path for thermal conduction. Greater powder packing density (*e.g.*, resulting from a more spherical morphology) would result in greater thermal diffusion.

Micrographs of the two powders, Figure 13, indicate significant differences in the morphology and size of the two powders. The chemically reduced powder was found to have an irregular, faceted morphology with flake and rod structures in addition to small satellite particles and agglomerates. The plasma spheroidized powder had a highly spherical morphology with some small irregularities present on the particle surface. As neither powder was produced from a gas atomization process, internal pores were not expected.

Both powders show similar size ranges (Figure 14), although there is a plateau in the distribution for the plasma spheroidized powder from around 6 to 20 μm ; over this size range the chemically reduced powder has a cumulative percentage of 44. The greater proportion of fines would give a greater tendency to agglomerate, consistent with the SEM micrographs (Figure 13) along with the poorer flowability of the powder compared to the plasma spheroidized powder (Table IV). The poorer flowability shown by the chemically reduced powder would be expected to lead to greater variability of powder packing in the powder bed, which will be discussed below. A wider size distribution might be expected to result in greater packing density, but the morphology effects outweigh this tendency resulting in lower apparent density values (see Table IV). The single density value, however, does not represent the likely range experienced in a powder bed.

Higher density values are associated with higher thermal diffusivity values and so faster thermal transport in the plasma spheroidized powder build would be expected; the more insulating nature of the chemically reduced powder would then give higher temperatures in the powder layer. Analysis of the structure of the builds indicates that lack of fusion defects (see Figure 8) is more numerous for the chemically reduced powder build than for the plasma spheroidized powder build. Thus, although thermal diffusivity effects would lead to higher local temperatures for a similar heat input, the build microstructure is indicative that local temperatures in the chemically reduced build are lower than in the plasma spheroidized build. This is consistent with reduced heat input in the chemically reduced powder build. Hence, despite the broad assumptions of the analysis above, the minimum effective laser absorptivity values determined are indicative of a much-reduced intake of energy from the laser for the chemically reduced powder bed than for the plasma spheroidized powder.

The determined minimum absorbed efficiency of 0.20 and 0.35 for the chemically reduced and plasma spheroidized powders, respectively, were significantly lower than that of previous studies.^[33,34] This is likely due to the values only accounting for energy in melting rather than for all increases in substrate temperature (to less than that of the melting temperature). Additionally,

the 30 μm layer thickness used during the fabrication process would lower the absorptivity in comparison to Trapp *et al.*^[20] where the layer thickness was three times greater allowing for multiple internal reflections.

Comparing the minimum effective absorptivity values for plasma spheroidized and chemically reduced powders, then the lower packing density of the latter would contribute to the decreased heat input.^[16,22] The importance of packing density can be inferred from the correlation between reduced penetration depth and large lack of fusion defects, (Figure 10). It is likely that the poorer flowability of the chemically reduced powder leads to reduced local packing density and hence reduced heat input. This results in less particle melting and so a lack of fusion defect, while less heat is transported into the substrate, accounting for the reduced penetration.

The difference in apparent density, Table IV, is only 22 pct, while that in the minimum laser absorptivity is 43 pct, indicating that density is unlikely to fully account for the reduced heat input. Further to the modeling reported in the literature,^[34] the presence of facets in the chemically reduced powder would increase the amount of laser energy reflected back to the environment. The use of penetration depth to determine minimum effective absorptivity means that a number of potential factors (*e.g.*, scan strategy and conductivity) are not isolated, but incorporated in a single global parameter (hence the ‘apparent’ absorptivity). Thus, the approach and calculation do not have the sensitivity of more complex modeling studies, such as by Khairallah *et al.* or the ability to cover the features summarized in Reference 35. The use of penetration depth, particularly if single layer runs are made where powder layer thickness can be verified, is a rapid intermediate step between the simple AED values and a multi-parameter simulation.

The trends seen, in terms of increased packing density increasing laser absorptivity and increased sphericity increasing laser absorptivity, are consistent between studies,^[10,16,20,34] while absolute values vary significantly depending on morphology and size distribution. This indicates the morphology of the powder is a key factor in its absorptivity but also indicates a need to identify the absorptivity of the powder used in each study as literature values are inconsistent. It also highlights the need for further work in this area to clarify a consistent method for absorptivity measurements and thus improve comparisons of values between powders of different morphologies or different material systems.

V. CONCLUSION

Build plate analysis to determine the penetration depth of the fusion zone was used to compare the minimum effective energy absorbed between powders of the same material system. The melt penetration for the samples produced by the plasma spheroidized powder was almost double that of the chemically reduced powder and related to minimum absorption efficiencies

of 0.44 and 0.26, respectively. This overcame some of the problems with previous laser absorption experiments which failed to produce representative packing.

The plasma spheroidized powder produced samples of enhanced quality with an average 7 pct higher density than their chemically reduced counterparts over a range of parameters as a result of the enhanced absorbed energy. Variations in penetration depth have been related to adjacent lack of fusion defects and related to local density and heat input.

ACKNOWLEDGMENTS

This project has received funding from the European Union's Horizon 2020 research and innovation program under Grant Agreement Number 633053 and support from the RCUK Energy Programme [Grant Number EP/I501045].

OPEN ACCESS

This article is licensed under a Creative Commons Attribution 4.0 International License, which permits use, sharing, adaptation, distribution and reproduction in any medium or format, as long as you give appropriate credit to the original author(s) and the source, provide a link to the Creative Commons licence, and indicate if changes were made. The images or other third party material in this article are included in the article's Creative Commons licence, unless indicated otherwise in a credit line to the material. If material is not included in the article's Creative Commons licence and your intended use is not permitted by statutory regulation or exceeds the permitted use, you will need to obtain permission directly from the copyright holder. To view a copy of this licence, visit <https://creativecommons.org/licenses/by/4.0/>.

REFERENCES

1. PLANSEE, *Tungsten*, <http://www.plansee.com/en/materials/tungsten.html>; Accessed 1/11/19.
2. N.P. Taylor and R. Pampin: *Fusion Eng. Des.*, 2006, vol. 81 (8), pp. 1333–38.
3. E.M. Savitskii and G.S. Burkhanov: *Physical Metallurgy of Refractory Metals and Alloys*, Consultants Bureau, New York, 1970.
4. H. He, Y. Zeng, and N. Qu: *Precis. Eng.*, 2016, vol. 45, pp. 285–91.
5. C.W. Corti: *Platin. Met. Rev.*, 1986, vol. 30 (4), pp. 184–95.
6. R.D. Li, J.H. Liu, Y.S. Shi, L. Zhang, and M.Z. Du: *Powder Metallurgy*, 2010, vol. 53 (4), pp. 310–17.
7. R.D. Li, Y.S. Shi, J.H. Liu, Z. Xie, and Z.G. Wang: *The International Journal of Advanced Manufacturing Technology*, 2010, vol. 48 (5), pp. 597–605.
8. D. Faidel, D. Jonas, G. Natour, and W. Behr: *Addit. Manuf.*, 2015, vol. 8, pp. 88–94.
9. D. Zhang, Q. Cai, and J. Liu: *Mater. Manuf. Process.*, 2012, vol. 27 (12), pp. 1267–70.

10. D. Wang, C. Yu, X. Zhou, J. Ma, W. Liu, and Z.J. Shen: *Appl. Sci.*, 2017, vol. 7 (4), pp. 430–42.
11. A. Iveković, N. Omidvari, B. Vrancken, K. Lietaert, L. Thijs, K. Vanmeensel, J. Vleugels, and J.-P. Kruth: *Int. J. Refract. Met. Hard Mater.*, 2018, vol. 72, pp. 27–32.
12. A.B. Spierings, M. Schneider, and R. Eggenberger: *Rapid Prototyping Journal*, 2011, vol. 17 (5), pp. 380–86.
13. M. Joyce: *Nuclear Engineering: A Conceptual Introduction to Nuclear Power*, 1st ed., Butterworth-Heinemann, Oxford, 2017.
14. D. Schulze, *Flow Properties of Powders and Bulk Solids*. (2006), <http://www.dietmar-schulze.com/grdle1.pdf>; Accessed 1/11/19.
15. F.A.L. Dullien, *Porous Media*, ed. H. Brenner, 2nd ed., Academic Press, Massachusetts, U.S.A., 1991.
16. R.L. Carr: *Chem. Eng. J.*, 1965, vol. 72, pp. 163–68.
17. Y. Lee and W. Zhang: *26th Solid Freeform Fabrication*, University of Texas, Austin, 1999, pp. 1154–65.
18. J.H. Tan, W.L.E. Wong, and K.W. Dalgarno: *Addit. Manuf.*, 2017, vol. 18, pp. 228–55.
19. N.P. Karapatis, G. Egger, P.-E. Gyax, and R. Glardon: *26th Solid Freeform Fabrication Symposium*, University Texas, Austin, 1999, pp. 255–63.
20. J. Trapp, A.M. Rubenchik, G. Guss, and M.J. Matthews: *Appl. Mater. Today*, 2017, vol. 9 (Supplement C), pp. 341–49.
21. C.D. Boley, S.C. Mitchell, A.M. Rubenchik, and S.S.Q. Wu: *Applied Optics*, 2016, vol. 55 (23), pp. 6496–6500.
22. A.V. Gusarov and E.P. Kovalev: *Phys. Rev. B*, 2009, vol. 80 (2), pp. 024202-1–024202-15.
23. *Oxygen, Nitrogen, and Hydrogen in Refractory Metals*, Leco Corporation, http://www.leco.co.za/wp-content/uploads/2012/12/ONH836_O-N-H_REFRACTORY_METALS_203-821-427.pdf; Accessed 1/11/19.
24. *Standard Test Method for Particle Size Distribution of Catalytic Materials by Laser Light Scattering*, ASTM International, West Conshohocken, PA., 2015.
25. *Standard Test Method for Bulk Solids Using Schulze Ring Shear Tester*, ASTM International, West Conshohocken, PA., 2016.
26. *Standard Test Method for Apparent Density of Free-Flowing Metal Powders Using the Hall Flowmeter Funnel*, ASTM International, West Conshohocken, PA., 2013.
27. *Standard Test Method for Determination of Tap Density of Metal Powders and Compounds*, ASTM International, West Conshohocken, PA., 2015.
28. *Standard Test Methods for Density of Compacted or Sintered Powder Metallurgy (PM) Products Using Archimedes' Principle*, ASTM International, West Conshohocken, PA., 2015.
29. J. Schindelin, I. Arganda-Carreras, E. Frise, V. Kaynig, M. Longair, T. Pietzsch, S. Preibisch, C. Rueden, S. Saalfeld, B. Schmid, J.-Y. Tinevez, D.J. White, V. Hartenstein, K. Eliceiri, P. Tomancak, and A. Cardona: *Nat. Methods*, 2012, vol. 9, pp. 676–82.
30. E. Lassner and W.D. Schubert: *Tungsten: Properties, Chemistry, Technology of the Element, Alloys, and Chemical Compounds*, Plenum Publishers, New York, 1999, pp. 1–59.
31. S.W.H. Yih and C.T. Wang: *Tungsten: Sources, Metallurgy, Properties, and Applications*, Plenum Press, New York, 1979, p. 256.
32. A. Thompson and B.N. Taylor: *Guide for the use of the International System of Units (SI)*. 2010, Maryland, U.S.A., <http://www.nist.gov/phylab/pubs/sp811/index.cfm>. Accessed 1/11/19.
33. D. Bergström, The Absorption of Laser Light by Rough Metal Surfaces, in *Applied Physics and Mechanical Engineering* (2008), PhD thesis, Luleå University of Technology, Österund, Sweden.
34. C.D. Boley, S.A. Khairallah, and A.M. Rubenchik: *Appl. Opt.*, 2015, vol. 54 (9), pp. 2477–82.
35. *Additive Manufacturing Handbook, 2017*, 1st ed., A.B. Badim, and V.V. Valencia, and D. Liu, eds., *Additive Manufacturing Handbook, 2017*, CRC Press, Boca Raton, FL, 2017 Chapters 7, 15 and 27.

Publisher's Note Springer Nature remains neutral with regard to jurisdictional claims in published maps and institutional affiliations.